Article

Scanning Tunneling Microscopy of Bimetallic Ni/Co-HITP Metal−Organic Framework Monolayers

Fubiao Gu,[†] Sisheng Shu,[†] Christopher E. Patrick, and Martin R. Castell*

Cite This: *J. Phys. Chem. C* 2024, 128, 17797−17805

Read Online

ACCESS | Metrics & More | Article Recommendations

ABSTRACT: Metals (Ni, Co) and hexaaminotriphenylene (HATP) molecules are evaporated separately in an ultrahigh vacuum onto the Au(111) surface. During an annealing step, monolayer single metal and bimetallic $Ni_xCo_{3-x}(HITP)_2$ metal−organic frameworks (MOFs) are formed via an on-surface reaction of the organic molecules with the metals. The MOFs are characterized by scanning tunneling microscopy (STM), which reveals the hexagonal framework structures and growth processes. The pure $Ni_3(HITP)_2$ and bimetallic $Ni_xCo_{3-x}(HITP)_2$ frameworks have a similar isotropic island morphology, while the $Co_3(HITP)_2$ islands are ribbon shaped. Individual Ni and Co metal centers can be atomically identified by their different apparent heights in the STM images of the bimetallic framework. Density functional theory (DFT) calculations indicate that the apparent height difference is caused by electronic effects rather than the difference of topography. The STM images further reveal that in the mixed-metal MOFs the Ni and Co centers are distributed randomly.
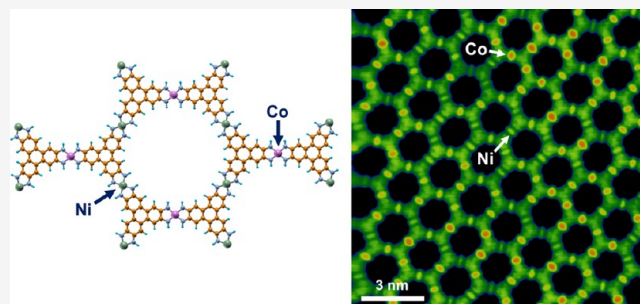
1. INTRODUCTION

The family of metal−organic frameworks (MOFs) with $M_3(HXTP)_2$ stoichiometry (M = transition metals; HXTP = 2,3,6,7,10,11-hexa-substituted triphenylenes) was first reported in 2012.[1] These MOFs are made from near-planar-squarely coordinated metals and trinucleating bidentate planar ligands and form hexagonal honeycomb structures. They are of technological interest because of their high electrical conductivities and can therefore be used in chemiresistive sensors,[2,3] supercapacitors,[4,5] electrocatalysts,[6,7] superconductors,[8,9] and transistors.[10,11] $M_3(HXTP)_2$ MOFs are often referred to as "two-dimensional (2D) MOFs" because of their planar structure but the majority of the materials that have been synthesized through solution-based techniques consist of stacked van der Waals-bonded layers, resulting in three-dimensional (3D) materials. It is possible to create single-molecule-thickness 2D layers by vacuum growth techniques such as chemical vapor deposition and on-surface synthesis.[12−15] This approach can be used for the fabrication of a variety of supramolecular structures on surfaces, including one-dimensional (1D) chains and 2D networks, and enables the chemical and physical properties of these low-dimensional structures to be studied at their single-layer limit.[16−23]

The properties of MOFs can be tuned by creating alloys of the organic ligands or the metal centers. Wu et al. used an HHTP/HATP dual-ligand strategy to grow Cu-MOFs and achieved an enhanced selectivity for chemiresistive sensing.[24] Lian and colleagues made a series of bimetallic Ni/Co-HITP-

MOFs which bridge the gap of crystallinity, conductivity, and oxygen reduction reaction (ORR) activity between pure $Ni_3(HITP)_2$ and $Co_3(HITP)_2$ (HITP is the deprotonated/dehydrogenated imine form of HATP).[25] Dincǎ's group investigated Ni/Co, Ni/Cu, and Co/Cu-HITP bimetallic MOFs and observed a continuous tunability of bandgap and electrical conductivity.[26] To determine how the metal centers are distributed in bimetallic MOFs is a difficult characterization challenge that cannot be tackled by techniques such as transmission electron microscopy. However, under advantageous imaging conditions, scanning probe microscopy methods are able to identify the molecules and metal centers.[15]

Here, we report the synthesis of monolayer MOFs in an ultrahigh vacuum (UHV) by separately evaporating HATP molecules and Ni and/or Co onto the Au(111) surface. Annealing these samples provides sufficient thermal energy for diffusion and on-surface chemical reactions to take place. The HATP (hexa**amino**triphenylene) molecules when fully coordinated with Ni or Co will have lost six hydrogen atoms and hence become HITP (hexa**imino**triphenylene) molecules
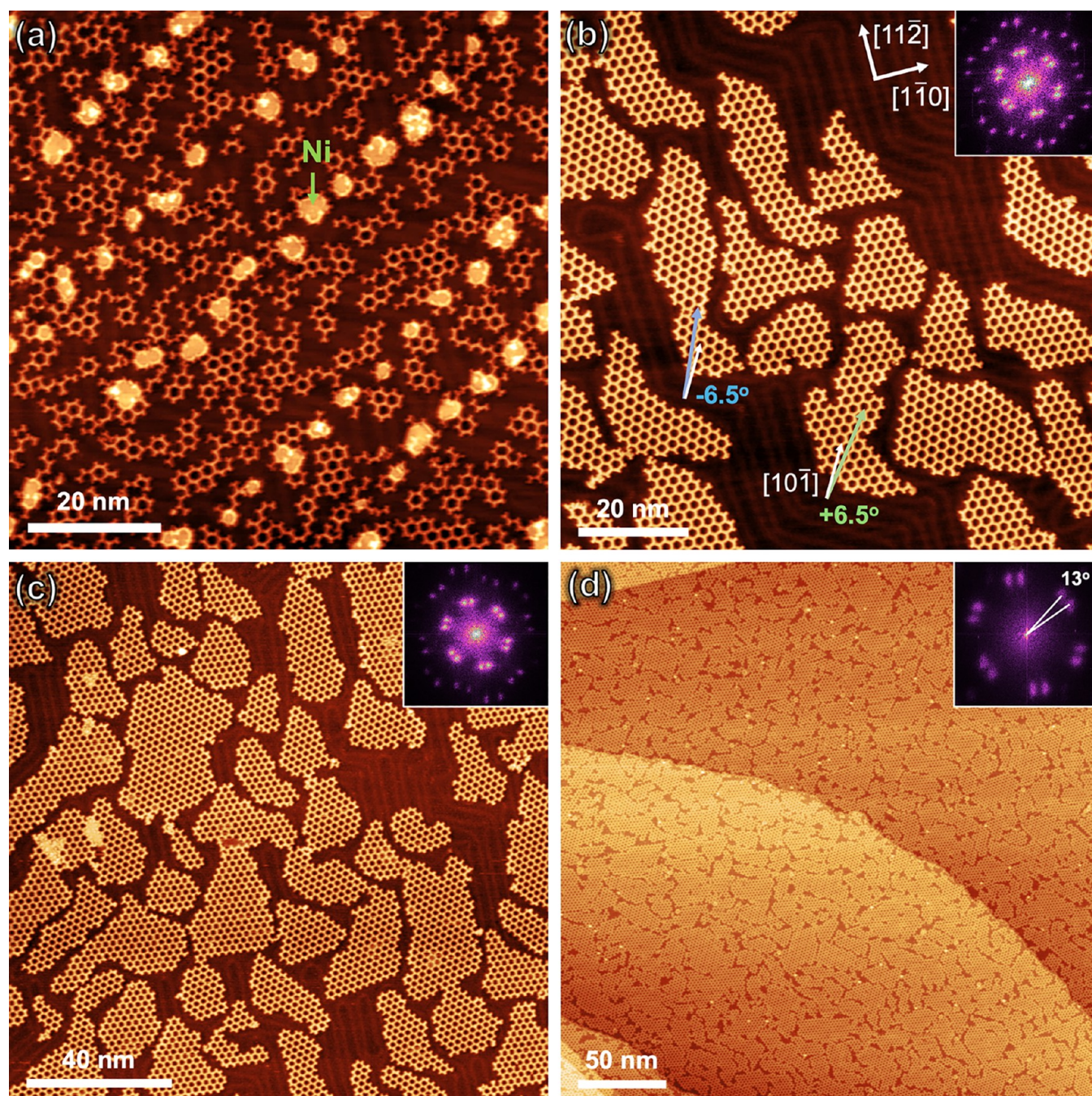
Figure 1. (a) STM image of the Au(111) surface following the deposition of Ni and HATP and an anneal at 180 °C. Hexagonal clusters showing the initial steps of polymerization are seen. $V_s = -1.0$ V, $I_t = 0.15$ nA, 10 frames averaged. (b) $Ni_3(HITP)_2$ MOFs created following 250 °C annealing. Honeycomb domains with two orientations are seen, as labeled by the green and blue arrows. The Au(111) herringbone reconstruction can be seen between the MOF domains. $V_s = -1.0$ V, $I_t = 0.15$ nA, 13 frames averaged. (c) Extended $Ni_3(HITP)_2$ domains with the honeycomb structure. $V_s = 1.0$ V, $I_t = 0.15$ nA, 3 frames averaged. (d) Maximum-coverage $Ni_3(HITP)_2$ MOF (~0.86 ML) obtained following repeated cycles of Ni/HATP deposition and annealing. $V_s = -1.0$ V, $I_t = 0.15$ nA. The insets in parts (b–d) are the FFTs of the STM images.

within the MOF. Using scanning tunneling microscopy (STM), we are able to follow the evolution of the growth for the $Ni_3(HITP)_2$ and $Co_3(HITP)_2$ MOFs and compare these with bimetallic $Ni_xCo_{3-x}(HITP)_2$ MOFs. Our high-resolution STM images enable us to distinguish the atomic Ni and Co metal centers in the bimetallic MOF and find that the metal centers are randomly distributed. Our STM image interpretation of the metal centers is also confirmed through density functional theory (DFT) simulations.

2. MATERIALS AND METHODS

All experiments were carried out in the UHV chambers of a JEOL-4500s STM. STM images were taken in a constant current mode at room temperature under UHV (10^{-8} Pa) with an electrochemically etched W tip. The substrates that were used were Au(111) thin films on mica (300 nm thickness, Unisoku) and were sputter-cleaned by an Ar$^+$ gun (VG Microtech EX03) and annealed to 650 °C via a SrTiO$_3$ single crystal heater placed underneath the mica. Repeated sputter/
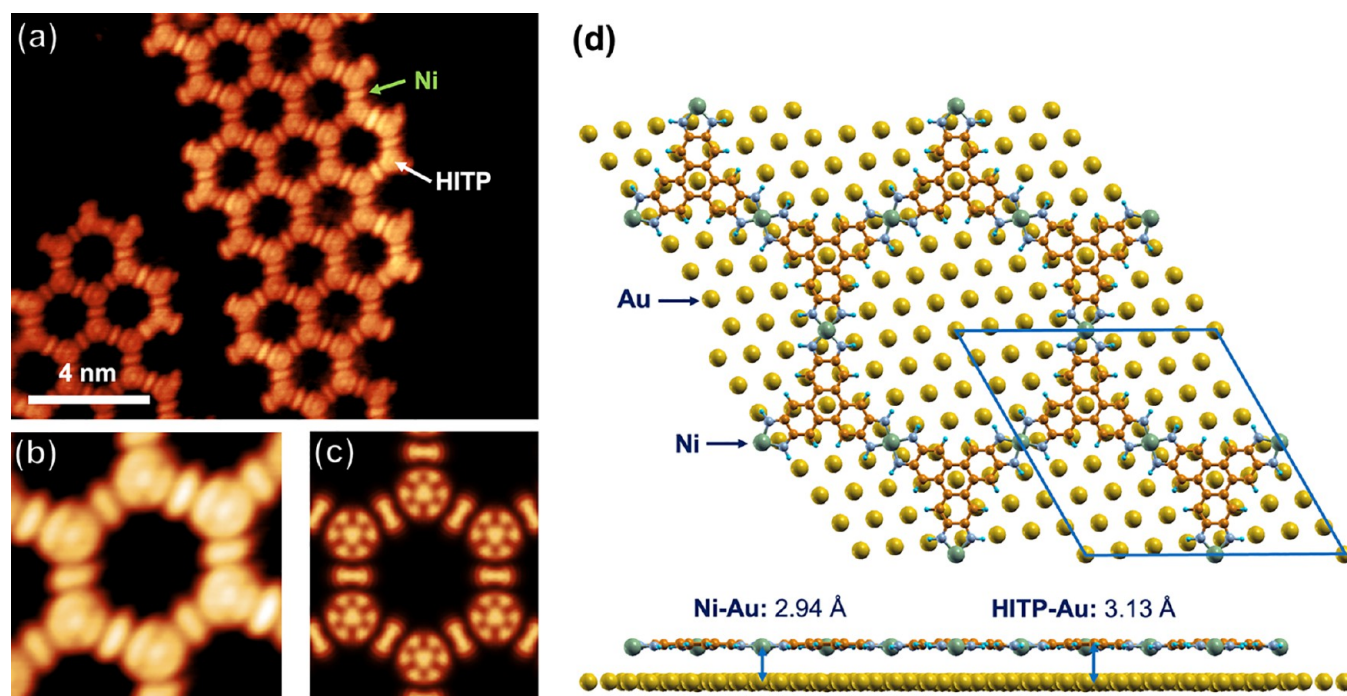
Figure 2. (a) STM image of the $Ni_3(HITP)_2$ honeycomb with submolecular resolution. $V_s = -1.0$ V, $I_t = 0.15$ nA, 7 frames average. (b) Averaged unit cell of the hexagon. (c) STM image simulation from DFT calculation at -1.0 V. (d) DFT-optimized structure of a $Ni_3(HITP)_2$ layer adsorbed on Au(111) (a three-layer slab, but only the top layer is shown for clarity). The $(\sqrt{57} \times \sqrt{57})$ unit cell is marked by the blue parallelogram. Ni: green, C: orange, N: blue-gray, H: light blue and Au: yellow.

anneal cycles resulted in the familiar herringbone reconstruction with a local $(22 \times \sqrt{3})$ unit cell. HATP molecules were synthesized following Chen's recipe,[27] further purified in UHV and sublimated at 250 °C in a CreaTec single filament effusion cell. Ni and Co were deposited from high-purity rods (99.99+%, Goodfellow) by an e-beam evaporator (Oxford Applied Research EGCO4). STM images were processed with *Gwyddion* and *Smart Align*. *Smart Align* is a multiframe averaging tool to improve the signal-to-noise ratio and the resolution of images through averaging a series of images that were obtained under the same imaging conditions.[28,29] Most STM images shown in this work are averaged over ~10 frames, and this information is included in the figure captions.

All density functional theory (DFT) calculations were carried out with the QUANTUM-ESPRESSO package.[30,31] The electron−ion interaction was described by ultrasoft pseudopotentials, and the electron wave functions and density were expanded in a plane-wave basis up to a maximum kinetic energy of 40 and 480 Ry, respectively.[32,33] Exchange and correlation were modeled using the Perdew−Burke−Ernzerhof (PBE) functional, with an empirical correction (Grimme-D3) included to account for weak van der Waals interactions.[34,35] The Au substrate was modeled as three atomic layers using the experimental lattice constant of 4.08 Å separated by a vacuum region of 15 Å. Subsequent fixed-cell structure optimizations were performed until the forces on each atom were smaller than 0.02 eV/Å with the bottom (the third) layer Au atoms fixed. The Brillouin zone was sampled using a $4 \times 4 \times 1$ Monkhorst−Pack k-point grid for self-consistent calculations, and a finer $8 \times 8 \times 1$ grid was used for density of states (DOS) calculations.[36] STM images were simulated within the Tersoff−Hamann approximation,[37] integrating the local DOS between the Fermi level and 1.0 V, and using a constant height plane located 3.4 Å above the MOFs.

3. RESULTS AND DISCUSSION

3.1. Growth of $Ni_3(HITP)_2$ MOF. Ni is evaporated onto the Au(111) surface and forms small islands at the elbow sites of the herringbone reconstruction. These can be seen in the STM image in Figure 1(a) and appear as regularly spaced bright regions of up to 5 nm in diameter. One of the Ni islands is indicated with an arrow in the figure. If HATP is evaporated onto a surface containing Ni, or vice versa, then HATP and Ni undergo complexation at room temperature, leading initially to a distribution of low-level polymers such as Ni-$(HATP)_2$ dimers. The HATP and Ni reaction is thought to occur via deprotonation of the amino group of the ligands. After low-temperature (180 °C) annealing, complexes in the shape of polygonal strings and small hexagonal clusters evolve (Figure 1a). These irregular structures grow both around the Ni islands and between them, demonstrating that the Ni metal is sufficiently mobile on the Au(111) surface at 180 °C to enable complexation to occur away from the Ni island nuclei. Through extended annealing to 250 °C, these hexagonal structures become enlarged to form regular honeycomb domains as shown in Figure 1b−d. We refer to these extended structures as $Ni_3(HITP)_2$ MOFs.

The average $Ni_3(HITP)_2$ domain size is around 30 nm × 30 nm (Figure 1c). Two epitaxial honeycomb orientations measured to be rotated ±6.5° with respect to the $\langle 110 \rangle$ directions of the Au(111) surface are found, as labeled by the green and light blue arrows in Figure 1b. The $\langle 110 \rangle$ surface directions can be determined by drawing lines perpendicular to the parallel rows of the herringbone reconstruction as indicated by white crystallography arrows toward the top of Figure 1b. The unit cell of the $Ni_3(HITP)_2$ network has a measured lattice constant of 2.16 ± 0.06 nm, close to the previously reported value.[38,39] A few repeated cycles of deposition of Ni
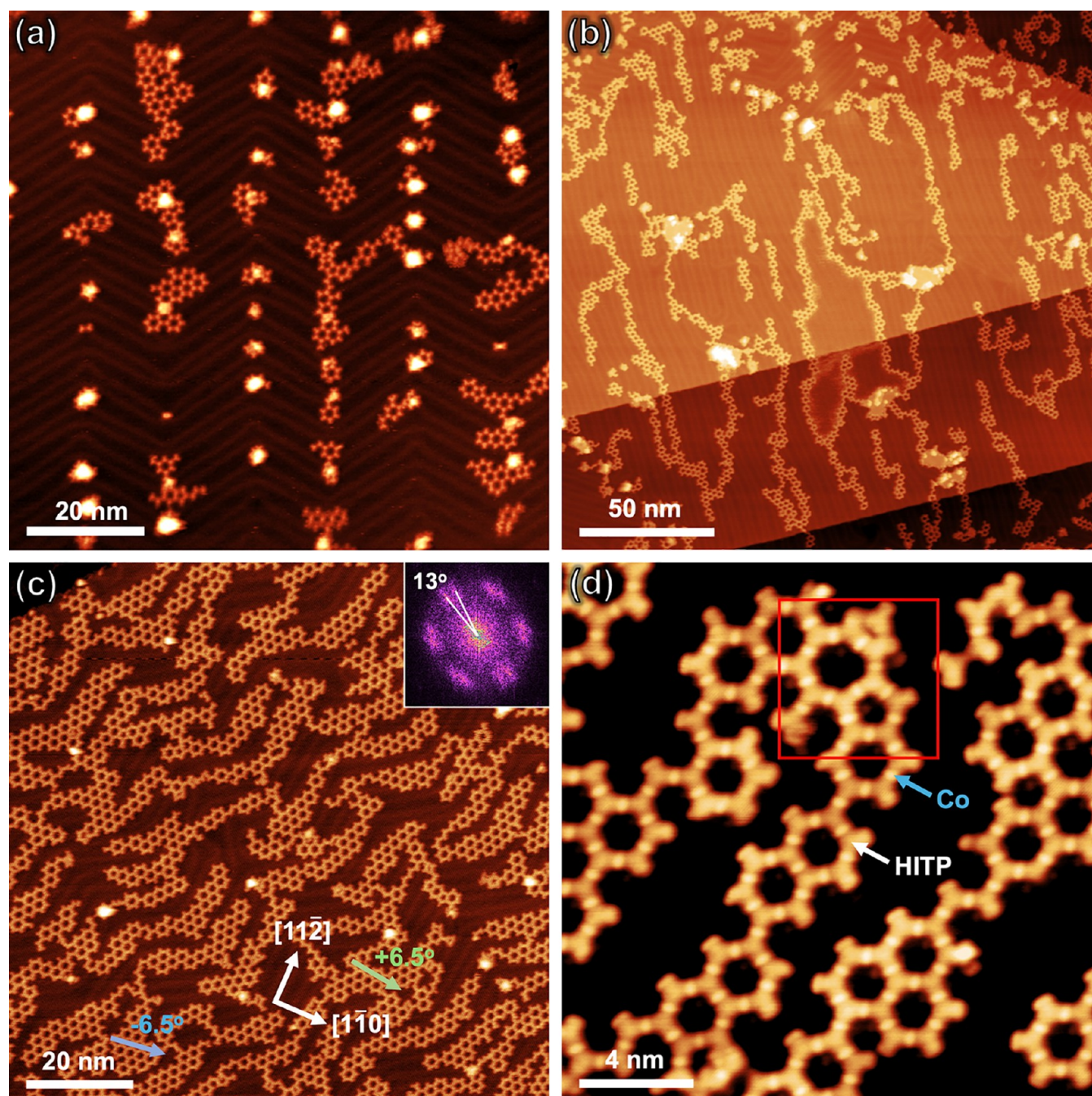
Figure 3. STM images of the Co-HATP MOF system. (a) STM image obtained after the deposition of Co and HATP onto the Au(111) substrate, followed by a 170 °C anneal. The bright dots in the image are due to Co-clustering at the herringbone elbow sites. Some low-level polymers are evident. V_s = 1.0 V, I_t = 0.15 nA. (b) Long Co-HATP polymer chains follow the lines of the herringbone reconstruction. V_s = −1.0 V, I_t = 0.10 nA. (c) Co-HATP nanoribbons obtained after annealing at 210 °C. The ±6.5° domain orientations are indicated. Inset: FFT analysis of the STM image. V_s = −1.0 V, I_t = 0.15 nA. (d) High-resolution image showing some pentagonal and heptagonal rings within the red border. The Co centers appear brighter than the ligands. V_s = −1.0 V, I_t = 0.15 nA, 12 frame average.

and HATP and annealing result in the highest monolayer coverage that we could achieve of around 86% (Figure 1d). The fast Fourier transforms (FFT) in the insets of the images in Figure 1(b−d) show the two distinct domain periodicities (2.16 nm) and the 13° rotation between them (±6.5°). We can use these measurements to establish the epitaxial relationship between the $Ni_3(HITP)_2$ network and the Au(111) substrate and have determined that the closest match is $(\sqrt{57} \times \sqrt{57})$-$R$ 6.587.° The $\sqrt{57}$ periodicity corresponds to a unit cell dimension of 2.178 nm and an angle

of rotation between the domains of 13.174°, which are both within the experimental error of the measurements of our STM images. The epitaxial arrangement of the $Ni_3(HITP)_2$ network on the Au(111) surface is shown in Figure 2d.

We attempted to prepare continuous single-domain MOF coverage of the surface, but this has proved challenging because of the apparently strong epitaxial interaction between the MOF layer and the Au(111) substrate. Once a domain of a particular orientation has formed, it does not readily change its orientation or shift laterally. This means that domain
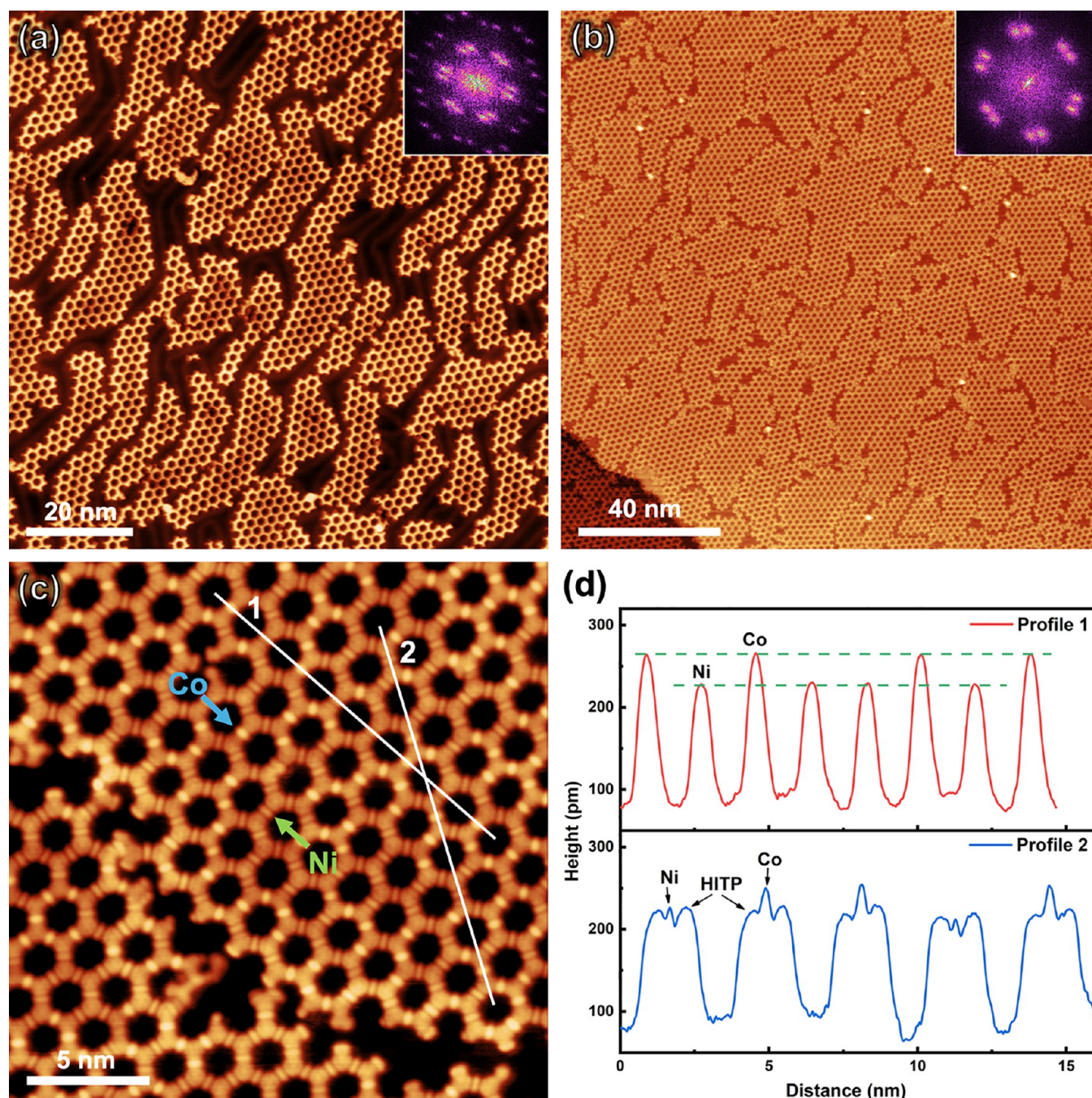
Figure 4. STM images of $Ni_xCo_{3-x}(HITP)_2$ bimetallic MOFs created by the co-deposition of Ni and Co followed by the deposition of HATP ligands with subsequent annealing. (a) MOF domains with $(\sqrt{57} \times \sqrt{57})\text{-}R\ 6.6°$ epitaxy as shown in the FFT inset. $V_s = -1.0$ V, $I_t = 0.10$ nA, 7 frame average. (b) High-coverage bimetallic MOF with an FFT inset. $V_s = -1.0$ V, $I_t = 0.07$ nA. (c) High-resolution STM image of the bimetallic MOF where the Co centers appear brighter than the Ni centers. $V_s = -1.0$ V, $I_t = 0.10$ nA, 20 frame average. (d) The two height profiles indicated in (c) are shown. The top profile 1 (red) through the metal centers shows that the Co features appear ∼30 pm higher than the Ni features. The bottom profile 2 (blue) through the metals centers and organic ligands shows that the Ni centers appear at the same height as the HITP molecules, while the Co centers are ∼30 pm higher.

agglomeration during annealing is not a feasible way to increase domain sizes. This only leaves domain ripening as a possible mechanism to increase domain sizes, however, ripening relies on the detachment of HITP from one domain and reattachment to another, and we have found that the temperatures where molecular detachment occurs are above those where the degradation of the network takes place (>500 °C). In one sense, the strong epitaxial interaction between the MOF and the Au(111) substrate has a positive effect in that it

promotes on-surface MOF synthesis. However, in another sense, the strong epitaxy also has negative ramifications because the two rotational domains and offsets between the islands prevent the formation of large area single-domain monolayer surface coverage.

Figure 2a is a high-resolution STM image that shows that under negative sample bias (filled electronic states) the NiN_4H_4 center appears like a rounded rectangle in the image and the triphenylene molecule appears as a broad circle with a
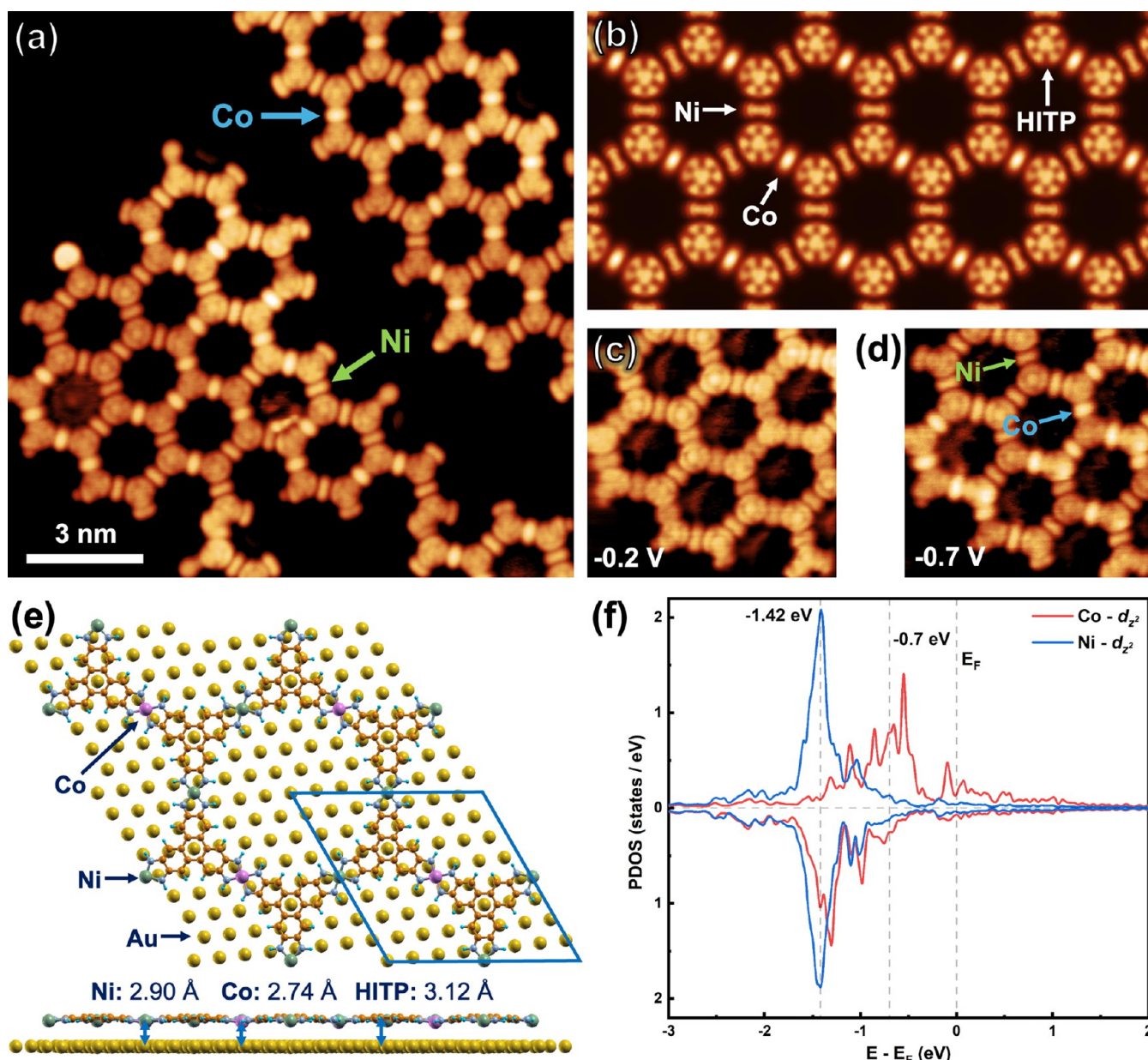
Figure 5. (a) STM image of a $Ni_xCo_{3-x}(HITP)_2$ bimetallic ($x \approx 1.7$) MOF with dim Ni and bright Co centers identified. $V_s = -1.0$ V, $I_t = 0.15$ nA, 17 frame average. (b) DFT simulation of STM image at -1.0 V for a $Ni_2Co(HITP)_2$ layer showing dim Ni and bright Co centers. (c) STM image of the bottom-left region of (a) but taken at -0.2 V sample bias. The Co and Ni centers cannot be distinguished at this voltage. 6 nm × 6 nm image, $V_s = -0.2$ V, $I_t = 0.15$ nA, 7 frame average. (d) The same region as (c) but taken at -0.7 V sample bias showing that this voltage is sufficient to distinguish the Ni and Co centers. 6 nm × 6 nm image, $V_s = -0.7$ V, $I_t = 0.15$ nA, 6 frame average. (e) DFT-optimized structure of a $Ni_2Co(HITP)_2$ layer adsorbed on Au(111). The top view shows the $(\sqrt{57} \times \sqrt{57})$-$R$ 6.6° epitaxy (blue parallelogram). The side view shows the different heights of the Ni, Co, and HITP units relative to the Au(111) substrate. Only the top-layer Au atoms are shown for the sake of clarity. Ni: green, Co: purple, C: orange, N: blue-gray, H: light blue and Au: yellow. (f) Projected density of states (PDOS) plots for the d_{z^2} orbitals of the Ni and Co atoms in the structures from (b, e). The Co atoms (red line) have a much stronger DOS nearer to the Fermi energy than the Ni atoms (blue).

dot in its center. The image in Figure 2b is a unit cell average of the image in (a). DFT calculations were performed to study the properties of this system. For a free-standing single-layer $Ni_3(HITP)_2$ MOF, the DFT-optimized lattice constant is 21.90 Å, close to the value measured in the experiment. The $Ni_3(HITP)_2$ MOF adopts a superstructure of $(\sqrt{57} \times \sqrt{57})$-$R$ 6.6° when adsorbed on Au(111). Figure 2d shows the optimized structure of the adsorbed system, with only the top layer of the Au(111) substrate shown for clarity. In this adsorption geometry each Ni atom is located at a "bridge" site,

and the central aromatic ring of the ligand is on a "top" site of the Au(111) substrate. In the side view of Figure 2d, we can see that the distance between the Ni atoms and the top-layer of Au atoms is 2.94 Å, while the HITP molecules have a slightly larger distance of 3.13 Å. The simulated STM image at -1.0 V is shown in Figure 2c and is qualitatively comparable with the STM image in (b).

3.2. Growth of Co-HITP MOF. If the metal source is switched to Co, we find that the same deposition and annealing processes as those used for Ni lead to different MOF

domain morphologies. Early-stage Co-HATP complexes are similar to the ones involving Ni, as shown in the STM image of hexagonal clusters in Figure 3a. However, these Co-HATP elements evolve into anisotropic nanoribbons after annealing. Usually, the length of the nanoribbons is around 30−40 nm, but they can reach up to 150 nm and readily cross the Au substrate step edges as shown in Figure 3b. The long direction of the ribbons appears to follow the orientation of the bright double rows of the Au(111) $(22 \times \sqrt{3})$ surface reconstruction as seen in Figure 3b,c, leading to extended ribbon growth if the rows are long and straight (Figure 3b) as opposed to their usual zigzag herringbone configuration (Figure 3c). The phenomenon of the Au(111) reconstruction driving the orientation of a hexagonal molecular overlayer has also been observed in other systems such as PTCDI-melamine networks.[23] The bright double rows of the Au(111) reconstruction are due to soliton walls that separate face-centered cubic (fcc) and hexagonal close-packed (hcp) terminations.[40] The fcc regions are slightly wider than the hcp regions, so it is possible to distinguish these regions in the STM images. Careful examination of Figure 3b and related images shows that the Co-MOF growth preferentially occurs in the fcc-terminated regions. To gain deeper insight into this observation, we compared the DFT-calculated adsorption energies of the Co-MOF on a slab of fcc versus hcp Au(111), but these calculations did not yield a difference. The only conclusion that can be drawn from this is that the soliton walls act as a barrier to Co-MOF growth and that the fcc regions are preferred because they are wider and therefore enable more extensive network formation.

The epitaxial relationship between Co-HATP and Au(111) is not generally as well-defined as that for the Ni-MOF because of the ribbon morphology. However, some ribbons are wide enough to enable an epitaxial classification, and for these, two orientational domains are also found. The orientations $(\pm 6.5°)$ are marked by the blue and green arrows in Figure 3c. The FFT in the inset of Figure 3c shows two blurred dots next to each other, resembling the patterns in Figure 1b−d. Based on periodicity measurements in the STM images and the FFT result, the $Co_3(HITP)_2$ MOF is determined to have the same $(\sqrt{57} \times \sqrt{57})$-$R$ 6.6° epitaxy as the Ni-MOF.

We also occasionally observe pentagonal and heptagonal rings in the Co-MOF ribbon structures. The highlighted red square in Figure 3d contains a seven-membered ring in the top part and a five-membered ring in the bottom part. We have not observed these types of defects in $Ni_3(HITP)_2$ honeycomb structures. This observation may indicate a stronger epitaxial interaction between the Ni-MOF and the Au(111) substrate compared with a weaker interaction for the Co-MOF. Apart from the morphology, another difference between the Ni-MOF and Co-MOF is that the Co centers appear notably brighter than the triphenylene ligands under certain STM imaging conditions (below −0.5 V sample bias), as can be seen in Figure 3d.

3.3. Growth of Bimetallic $Ni_xCo_{3−x}(HITP)_2$ MOFs. HITP-MOFs can be created by using two different metals in the synthesis step, resulting in bimetallic $M_xM'_{3−x}(HITP)_2$ MOFs. By adjusting the M/M′ ratio of the metals the MOF properties can be tuned.[26] Given the significantly different morphologies of the Ni and Co MOFs shown in the previous two sections, it was not obviously predictable which morphology would result when using two metal sources simultaneously. To explore this scenario, we evaporated Ni and

Co onto the Au(111) surface, which results in mixed NiCo clusters at the elbow sites. We then deposited HATP molecules and annealed the sample. Large-scale STM images of the resulting MOF islands are shown in Figure 4a,b. These islands have a similar morphology to the Ni-HITP-MOFs (Figure 1) and have the same $(\sqrt{57} \times \sqrt{57})$-$R$ 6.6° epitaxy. The two $\pm 6.5°$ orientations can be seen in the FFTs in the insets of Figure 4a,b. An open question remains, which is related to the distribution of the Ni and Co metal centers. A high-resolution STM image of the bimetallic MOF is shown in Figure 4c. The most striking aspect is that some of the metal centers appear significantly brighter than others. We assign this difference in brightness to whether the Ni−$(NH)_4$ or the Co−$(NH)_4$ metal center is being imaged. In Figure 3d, the Co centers appear brighter than the HITP molecules, whereas in Figure 2a, the Ni centers have approximately the same brightness as the HITP molecules. Using this argument, as annotated in the image, we assign in Figure 4c, the brighter metal centers to Co and the dimmer ones to Ni. Figure 4d shows the profiles indicated in Figure 4c in two directions where Co appears higher than Ni and HITP. During growth, the metals appear to be indiscriminately incorporated into the MOF, resulting in randomly distributed Ni and Co in the $Ni_xCo_{3−x}(HITP)_2$ domains.

In order to further investigate the apparent height difference in the STM images between the Ni and Co centers, we carried out DFT modeling of a $Ni_2Co(HITP)_2$ monolayer adsorbed on Au(111) with $(\sqrt{57} \times \sqrt{57})$-$R$ 6.6° epitaxy as shown in Figure 5e. The image simulation of this structure at −1.0 V is shown in Figure 5b. The STM image at −1.0 V (Figure 5a) and the simulation are a good qualitative match and support the interpretation that the bright metal centers are Co and the dim ones are Ni. A common question that arises in STM image interpretation is whether the differences in feature brightness are due to topographic or electronic effects. When viewing the MOF topography from the side (Figure 5e), it can be seen that the Ni atoms are located at 2.90 Å above the Au atoms, whereas the Co atoms are located lower at 2.74 Å. This means that topographically, the Ni atoms are 0.16 Å higher and hence favored for tunneling. However, the projected density of states (PDOS) plot of the d_{z^2} orbitals of Ni (blue) and Co (red) in the adsorbed MOF (Figure 5f) suggests that the Co metal centers dominate the energy window from −0.4 to −1.3 eV. The STM image simulation (Figure 5b) combines both topography and electronic structure and demonstrates that although the Co atoms are marginally lower topographically, they nevertheless appear brighter in the STM images due to their electronic structure. Compared with Ni^{2+}, Co^{2+} has an unpaired electron in the unhybridized d_{z^2} orbital, which is the main contributor to the PDOS prevalence and hence results in enhanced brightness in the STM images. Two images of part of the area in Figure 5a under biases of −0.2, and −0.7 V are compared in Figure 5c,d, demonstrating that it is necessary to include the peak in the d_{z^2} orbital DOS to be able to successfully discriminate between the Ni and Co centers. When the bias is −0.2 V, there is no obvious difference between the Ni and Co centers. After changing the bias to −0.7 V, the Co centers become brighter, in agreement with the PDOS plot (Figure 5f).

The PDOS of all of the metal d orbitals is shown in Figure 6. The first aspect that is evident is the asymmetric nature of the spin-up/spin-down contributions of the magnetic Co center versus the symmetric contributions of the nonmagnetic Ni
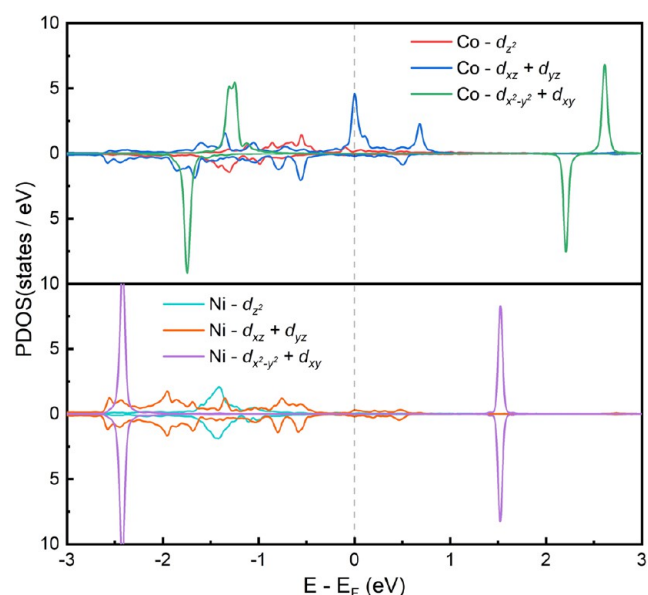
Figure 6. Projected densities of states (PDOS) for the *d* orbitals of the Co (top) and Ni (bottom) atoms in the Ni$_2$Co(HITP)$_2$−Au(111) system.

center. The largest peaks are for the in-plane d$_{x^2-y^2}$ and d$_{xy}$ orbitals; however, these orbitals do not have a significant impact on the STM images because they do not point toward the STM tip. The d$_{xz}$ and d$_{yz}$ orbitals have an out-of-plane contribution that points away from the surface, and this is especially large for the Co centers around the Fermi energy. However, according to the image simulations, it is the d$_{z^2}$ orbital that points directly toward the STM tip that dominates the image contrast.

4. CONCLUSIONS

Through the use of high-resolution STM imaging, we were able to reveal the differences in island morphology of isotropic Ni- and ribbon-shaped Co-HITP-MOFs. Simultaneous deposition of Ni and Co leads to bimetallic Ni$_x$Co$_{3-x}$(HITP)$_2$ MOFs, and by imaging these structures at below −0.7 V sample bias, we were able to identify bright Co centers and dim Ni centers that are distributed randomly in the networks. This knowledge is important for the interpretation of the properties of bimetallic MOFs where varying the metal ratio can be used to tune the functional properties. Further work on the nature of the magnetic Co centers and their interactions could be carried out with spin-polarized STM imaging to gain deeper insights into the electronic structure of this system.

■ AUTHOR INFORMATION

Corresponding Author

Martin R. Castell − *Department of Materials, University of Oxford, Oxford OX1 3PH, United Kingdom;* ⬤ orcid.org/0000-0002-4628-1456; Email: martin.castell@materials.ox.ac.uk

Authors

Fubiao Gu − *Department of Materials, University of Oxford, Oxford OX1 3PH, United Kingdom*

Sisheng Shu − *Department of Materials, University of Oxford, Oxford OX1 3PH, United Kingdom*

Christopher E. Patrick − *Department of Materials, University of Oxford, Oxford OX1 3PH, United Kingdom;* ⬤ orcid.org/0000-0002-1843-1269

Complete contact information is available at:
https://pubs.acs.org/10.1021/acs.jpcc.4c06050

Author Contributions

Notes

The authors declare no competing financial interest.

■ ACKNOWLEDGMENTS

■ REFERENCES

(1) Hmadeh, M.; Lu, Z.; Liu, Z.; Gándara, F.; Furukawa, H.; Wan, S.; Augustyn, V.; Chang, R.; Liao, L.; Zhou, F.; et al. New Porous Crystals of Extended Metal-Catecholates. *Chem. Mater.* **2012**, *24*, 3511−3513.

(2) Campbell, M. G.; Liu, S. F.; Swager, T. M.; Dincă, M. Chemiresistive Sensor Arrays from Conductive 2D Metal−Organic Frameworks. *J. Am. Chem. Soc.* **2015**, *137*, 13780−13783.

(3) Campbell, M. G.; Sheberla, D.; Liu, S. F.; Swager, T. M.; Dincă, M. Cu3(hexaiminotriphenylene)2: An Electrically Conductive 2D Metal−Organic Framework for Chemiresistive Sensing. *Angew. Chem., Int. Ed.* **2015**, *54*, 4349−4352.

(4) Sheberla, D.; Bachman, J. C.; Elias, J. S.; Sun, C.-J.; Shao-Horn, Y.; Dincă, M. Conductive MOF electrodes for stable supercapacitors with high areal capacitance. *Nat. Mater.* **2017**, *16*, 220−224.

(5) Feng, D.; Lei, T.; Lukatskaya, M. R.; Park, J.; Huang, Z.; Lee, M.; Shaw, L.; Chen, S.; Yakovenko, A. A.; Kulkarni, A.; et al. Robust and conductive two-dimensional metal−organic frameworks with exceptionally high volumetric and areal capacitance. *Nat. Energy* **2018**, *3*, 30−36.

(6) Clough, A. J.; Yoo, J. W.; Mecklenburg, M. H.; Marinescu, S. C. Two-Dimensional Metal−Organic Surfaces for Efficient Hydrogen Evolution from Water. *J. Am. Chem. Soc.* **2015**, *137*, 118−121.

(7) Jia, H.; Yao, Y.; Zhao, J.; Gao, Y.; Luo, Z.; Du, P. A novel two-dimensional nickel phthalocyanine-based metal−organic framework for highly efficient water oxidation catalysis. *J. Mater. Chem. A* **2018**, *6*, 1188−1195.

(8) Huang, X.; Zhang, S.; Liu, L.; Yu, L.; Chen, G.; Xu, W.; Zhu, D. Superconductivity in a Copper(II)-Based Coordination Polymer with Perfect Kagome Structure. *Angew. Chem., Int. Ed.* **2018**, *57*, 146−150.

(9) Takenaka, T.; Ishihara, K.; Roppongi, M.; Miao, Y.; Mizukami, Y.; Makita, T.; Tsurumi, J.; Watanabe, S.; Takeya, J.; Yamashita, M.; et al. Strongly correlated superconductivity in a copper-based metal-organic framework with a perfect kagome lattice. *Sci. Adv.* **2021**, *7*, No. eabf3996.

(10) Huang, X.; Sheng, P.; Tu, Z.; Zhang, F.; Wang, J.; Geng, H.; Zou, Y.; Di, C.-a.; Yi, Y.; Sun, Y.; et al. A two-dimensional π−d conjugated coordination polymer with extremely high electrical

conductivity and ambipolar transport behaviour. *Nat. Commun.* **2015**, *6*, No. 7408.

(11) Wu, G.; Huang, J.; Zang, Y.; He, J.; Xu, G. Porous Field-Effect Transistors Based on a Semiconductive Metal−Organic Framework. *J. Am. Chem. Soc.* **2017**, *139*, 1360−1363.

(12) Dong, L.; Gao, Z. A.; Lin, N. Self-assembly of metal−organic coordination structures on surfaces. *Prog. Surf. Sci.* **2016**, *91*, 101−135.

(13) Liu, J.; Abel, M.; Lin, N. On-Surface Synthesis: A New Route Realizing Single-Layer Conjugated Metal−Organic Structures. *J. Phys. Chem. Lett.* **2022**, *13*, 1356−1365.

(14) Liu, J.; Lin, N. On-Surface-Assembled Single-Layer Metal-Organic Frameworks with Extended Conjugation. *ChemPlusChem* **2023**, *88*, No. e202200359.

(15) Zhong, W.; Zhang, T.; Chen, D.; Su, N.; Miao, G.; Guo, J.; Chen, L.; Wang, Z.; Wang, W. Synthesizing Cr-Based Two-Dimensional Conjugated Metal-Organic Framework Through On-Surface Substitution Reaction. *Small* **2023**, *19*, No. 2207877.

(16) Heim, D.; Écija, D.; Seufert, K.; Auwärter, W.; Aurisicchio, C.; Fabbro, C.; Bonifazi, D.; Barth, J. V. Self-Assembly of Flexible One-Dimensional Coordination Polymers on Metal Surfaces. *J. Am. Chem. Soc.* **2010**, *132*, 6783−6790.

(17) Shi, Z.; Liu, J.; Lin, T.; Xia, F.; Liu, P. N.; Lin, N. Thermodynamics and Selectivity of Two-Dimensional Metallo-supramolecular Self-Assembly Resolved at Molecular Scale. *J. Am. Chem. Soc.* **2011**, *133*, 6150−6153.

(18) Denawi, H.; Nardi, E.; Koudia, M.; Siri, O.; Abel, M.; Hayn, R. Magnetic Polymer Chains of Iron and Zwitterionic Quinoidal Ligands on the Ag(111) Surface. *J. Phys. Chem. C* **2020**, *124*, 1346−1351.

(19) Liu, J.; Gao, Y.; Wang, T.; Xue, Q.; Hua, M.; Wang, Y.; Huang, L.; Lin, N. Collective Spin Manipulation in Antiferroelastic Spin-Crossover Metallo-Supramolecular Chains. *ACS Nano* **2020**, *14*, 11283−11293.

(20) Lin, T.; Kuang, G.; Shang, X. S.; Liu, P. N.; Lin, N. Self-assembly of metal−organic coordination networks using on-surface synthesized ligands. *Chem. Commun.* **2014**, *50*, 15327−15329.

(21) Gardener, J. A.; Shvarova, O. Y.; Briggs, G. A. D.; Castell, M. R. Intricate Hydrogen-Bonded Networks: Binary and Ternary Combinations of Uracil, PTCDI, and Melamine. *J. Phys. Chem. C* **2010**, *114*, 5859−5866.

(22) Mura, M.; Silly, F.; Burlakov, V.; Castell, M. R.; Briggs, G. A. D.; Kantorovich, L. N. Formation Mechanism for a Hybrid Supramolecular Network Involving Cooperative Interactions. *Phys. Rev. Lett.* **2012**, *108*, No. 176103.

(23) Silly, F.; Shaw, A. Q.; Briggs, G. A. D.; Castell, M. R. Epitaxial ordering of a perylenetetracarboxylic diimide-melamine supramolecular network driven by the Au(111)-(22x root 3) reconstruction. *Appl. Phys. Lett.* **2008**, *92*, No. 023102.

(24) Wu, A.-Q.; Wang, W.-Q.; Zhan, H.-B.; Cao, L.-A.; Ye, X.-L.; Zheng, J.-J.; Kumar, P. N.; Chiranjeevulu, K.; Deng, W.-H.; Wang, G.-E.; et al. Layer-by-layer assembled dual-ligand conductive MOF nano-films with modulated chemiresistive sensitivity and selectivity. *Nano Res.* **2021**, *14*, 438−443.

(25) Lian, Y.; Yang, W.; Zhang, C.; Sun, H.; Deng, Z.; Xu, W.; Song, L.; Ouyang, Z.; Wang, Z.; Guo, J.; Peng, Y. Unpaired 3d Electrons on Atomically Dispersed Cobalt Centres in Coordination Polymers Regulate both Oxygen Reduction Reaction (ORR) Activity and Selectivity for Use in Zinc−Air Batteries. *Angew. Chem., Int. Ed.* **2020**, *59*, 286−294.

(26) Chen, T.; Dou, J.-H.; Yang, L.; Sun, C.; Libretto, N. J.; Skorupskii, G.; Miller, J. T.; Dincă, M. Continuous Electrical Conductivity Variation in M3(Hexaiminotriphenylene)2 (M = Co, Ni, Cu) MOF Alloys. *J. Am. Chem. Soc.* **2020**, *142*, 12367−12373.

(27) Chen, L.; Kim, J.; Ishizuka, T.; Honsho, Y.; Saeki, A.; Seki, S.; Ihee, H.; Jiang, D. Noncovalently Netted, Photoconductive Sheets with Extremely High Carrier Mobility and Conduction Anisotropy from Triphenylene-Fused Metal Trigon Conjugates. *J. Am. Chem. Soc.* **2009**, *131*, 7287−7292.

(28) Jones, L.; Yang, H.; Pennycook, T. J.; Marshall, M. S. J.; Van Aert, S.; Browning, N. D.; Castell, M. R.; Nellist, P. D. Smart Align—a new tool for robust non-rigid registration of scanning microscope data. *Adv. Struct. Chem. Imaging* **2015**, *1*, No. 8.

(29) Jones, L.; Wang, S.; Hu, X.; Rahman, S. U.; Castell, M. R. Maximising the resolving power of the scanning tunneling micro-scope. *Adv. Struct. Chem. Imaging* **2018**, *4*, No. 7.

(30) Giannozzi, P.; Baroni, S.; Bonini, N.; Calandra, M.; Car, R.; Cavazzoni, C.; Ceresoli, D.; Chiarotti, G. L.; Cococcioni, M.; Dabo, I.; et al. QUANTUM ESPRESSO: a modular and open-source software project for quantum simulations of materials. *J. Phys.: Condens. Matter* **2009**, *21*, No. 395502.

(31) Giannozzi, P.; Andreussi, O.; Brumme, T.; Bunau, O.; Nardelli, M. B.; Calandra, M.; Car, R.; Cavazzoni, C.; Ceresoli, D.; Cococcioni, M.; et al. Advanced capabilities for materials modelling with Quantum ESPRESSO. *J. Phys.: Condens. Matter* **2017**, *29*, No. 465901.

(32) Vanderbilt, D. Soft self-consistent pseudopotentials in a generalized eigenvalue formalism. *Phys. Rev. B* **1990**, *41*, 7892−7895.

(33) Garrity, K. F.; Bennett, J. W.; Rabe, K. M.; Vanderbilt, D. Pseudopotentials for high-throughput DFT calculations. *Comput. Mater. Sci.* **2014**, *81*, 446−452.

(34) Perdew, J. P.; Burke, K.; Ernzerhof, M. Generalized Gradient Approximation Made Simple. *Phys. Rev. Lett.* **1996**, *77*, No. 3865.

(35) Grimme, S.; Antony, J.; Ehrlich, S.; Krieg, H. A consistent and accurate ab initio parametrization of density functional dispersion correction (DFT-D) for the 94 elements H-Pu. *J. Chem. Phys.* **2010**, *132*, No. 154104.

(36) Monkhorst, H. J.; Pack, J. D. Special points for Brillouin-zone integrations. *Phys. Rev. B* **1976**, *13*, No. 5188.

(37) Tersoff, J.; Hamann, D. R. Theory of the scanning tunneling microscope. *Phys. Rev. B* **1985**, *31*, No. 805.

(38) Gao, Z. A.; Hsu, C.-H.; Liu, J.; Chuang, F.-C.; Zhang, R.; Xia, B.; Xu, H.; Huang, L.; Jin, Q.; Liu, P. N.; Lin, N. Synthesis and characterization of a single-layer conjugated metal−organic structure featuring a non-trivial topological gap. *Nanoscale* **2019**, *11*, 878−881.

(39) Sheberla, D.; Sun, L.; Blood-Forsythe, M. A.; Er, S.; Wade, C. R.; Brozek, C. K.; Aspuru-Guzik, A.; Dincă, M. High Electrical Conductivity in Ni3(2,3,6,7,10,11-hexaiminotriphenylene)2, a Semi-conducting Metal−Organic Graphene Analogue. *J. Am. Chem. Soc.* **2014**, *136*, 8859−8862.

(40) Li, P.; Ding, F. Origin of the herringbone reconstruction of Au(111) surface at the atomic scale. *Sci. Adv.* **2022**, *8*, No. eabq2900.

■ **NOTE ADDED AFTER ASAP PUBLICATION**

This paper was published ASAP on September 27, 2024. Minor changes were made in the article. The corrected version was reposted on October 1, 2024.